

Modelling rock fracturing by a novel implicit continuous to discontinuous method

Bin Gong^a, Tao Zhao^{a,*}, Indrasenan Thusyanthan^b, Chun'an Tang^c

^a Department of Civil and Environmental Engineering, Brunel University London, London UB8 3PH, UK

^b Gavin & Doherty Geosolutions, London W1W 7LT, UK

^c State Key Laboratory of Coastal & Offshore Engineering, Dalian University of Technology, Dalian 116024, China

ARTICLE INFO

Keywords:

Continuous to discontinuous method
Rock fracturing
Progressive slope failure
Factor of safety
Rock heterogeneity

ABSTRACT

This research introduces a novel implicit continuous to discontinuous method to investigate the cross-scale failure process of discontinuous rock masses, including fine fracture creation, propagation, and rigid block contact. This method enables an intact rock to split and crush, with the local deformation/movement propagating rapidly throughout the whole system. The method was applied to investigate the progressive slope failure. The results revealed that the number of failure elements within the slope increased rapidly at the primary fracture stage. The upper part of the failure band gradually shifted upward and backward towards the slope crest, where several tension cracks were clearly visible. Additionally, the failed zone became wider as the homogeneity coefficient m increased. Furthermore, the factor of safety (FoS) increased as the growth stage of m progressed, but it reached a constant value when m exceeded 8, indicating that the material became relatively uniform. Interestingly, for slopes with varying elevation heights, the FoS decreased in a power function form as the ratio of the slope height to the width of the slope top surface increased. Overall, these findings shed light on developing the continuous-discontinuous computational model, with the application to study the progressive failure process of slopes.

1. Introduction

Geological disasters caused by rock failure are responsible for numerous casualties and economic losses worldwide. With an increasing number of infrastructures being built or designed in complex geological conditions, it is crucial to adopt multiple technical measures to ensure smooth project implementation. For instance, the construction of the Sichuan-Tibet Railway, which spans 1,838 km, reaches an altitude of 4,400 m, and an elevation difference of over 3,000 m, involves crossing several great rivers and eight huge mountains with abnormally active tectonic movement. Furthermore, the increasing exploitation and utilization of deep underground space and resources, such as coal, metal, and geothermal, necessitate new failure analysis models to account for observed characteristic mechanical behaviors of deep rocks (Deng et al., 2022; Luo and Gong, 2022; Ma et al., 2022; Zhang et al., 2022), such as zonal disintegration. In these engineering practices, the creation, penetration, and propagation of cracks have posed a significant challenge in the field of rock mechanics (Feng et al., 2022; Chen et al., 2022; Wang et al., 2022a) due to the complex nature of rock media.

Rock materials in nature are characterized by various defects such as voids, fissures, and cracks at micro, meso, and macro levels, which result from tectonic movements, internal liquid and gaseous substances, and long-term weathering and erosion. These complex and heterogeneous features make it difficult for conventional physical and mathematical models to accurately represent them. At the macro level, natural rock masses are often characterized by discontinuous structural planes that play a critical role in determining their mechanical response by providing potential slipping paths. Additionally, construction disturbances such as tunnel boring, hydraulic fracturing, and blasting can induce internal fracture development and weaken the strength of engineered rock masses (Liang et al., 2014; Chen et al., 2018a; Chen et al., 2018b; Gong et al., 2022), making the study of their nonlinear mechanical behaviors even more complex and variable.

Over the past few decades, several effective methods have been developed for determining the safety indices of rock structures, which can be classified into four categories: (1) practical methods based on industry standards or expert experience, (2) qualitative assessment methods based on rock mass classification or highly-generalized

* Corresponding author.

E-mail address: tao.zhao@brunel.ac.uk (T. Zhao).

<https://doi.org/10.1016/j.compgeo.2023.106035>

Received 27 July 2023; Received in revised form 24 November 2023; Accepted 18 December 2023

Available online 23 December 2023

0266-352X/© 2023 The Author(s). Published by Elsevier Ltd. This is an open access article under the CC BY license (<http://creativecommons.org/licenses/by/4.0/>).

theoretical formulae, (3) methods that draw detailed conclusions using data analysis systems or traditional numerical techniques, and (4) methods that obtain in-depth conclusions using advanced numerical techniques or artificial intelligence. However, the safe and stable state of rock structures is not only dependent on the rock matrix but also on the discontinuous structural planes. Therefore, many researchers have proposed theories and analysis models, among which limit analysis methods for determining the ultimate load of slopes, such as the Morgenstern-Price method (Morgenstern and Price, 1965), the Bishop method (Bishop, 1955), the Spencer method (Spencer, 1967), the Swedish method (Fellenius, 1936), and the Janbu method (Janbu, 1973), are representative examples. The application of these methods in practice is highly limited as some preconditions must be set in advance, such as the distribution law of internal forces, the division of slope strips, and the shape and position of the slipping surface. Additionally, as rock masses are complex geological materials, closed-form solutions do not exist for them, requiring the development of more powerful calculation technologies to accurately determine the safety indices of rock structures.

Numerous numerical methods have been developed to simulate the stress, deformation, and failure mode of rocks and rock masses. The continuum methods, including the finite element method (FEM) (Rutqvist et al., 2001) and the extended/generalized finite element method (XFEM/GFEM) (Fries and Belytschko, 2010; Strouboulis et al., 2000; Strouboulis et al., 2001), the finite difference/volume method (FDM/FVM) (Fallah et al., 2000; Wheel, 1996; Rodrigo et al., 2015), the boundary element method (BEM) (Brady and Bray, 1978), the rock failure process analysis method (RFPA) (Tang, 1997; Wang et al., 2022b; Yu et al., 2022), and the meshless method (MLM) (Zhang et al., 2000; Belytschko et al., 2000; Li et al., 2001), have made significant contributions to the field. However, these methods have limitations in modeling structural planes, although incorporating joint elements (Goodman et al., 1968; Goodman, 1976; Ghaboussi et al., 1973), fracture mechanics (Rybicki and Kanninen, 1977; Rice, 1968), or damage mechanics (Kachanov, 1999) can overcome some of these limitations. Nevertheless, new issues such as remeshing, robustness, and convergence arise with these approaches (Deb et al., 2015). To investigate the effect of discontinuities, such as natural joints, fissures, and bedding (Harrison and Hudson, 1997), various discontinuum methods have been proposed, including the discrete element method (DEM) (Cundall, 1971), the discrete fracture mesh method (DFN) (Long et al., 1982; Long et al., 1985; Robinson, 1984), the discontinuous deformation analysis (DDA) (Shi, 1988), and the manifold element method (NMM) (Yang et al., 2018; Zhang et al., 2018; Guo et al., 2019; Li et al., 2021). However, these methods have limitations in accurately calculating the fine stress/strain field and cross-scale fracture growth inside blocks/particles and may suffer from poor computational efficiency and parallel performance.

Additionally, several coupling approaches have been developed to model rock fracturing (Chen et al., 2022). For example, Xiang et al. (2022) simulated the rock erosion during water jet drilling using an immersed-body method. Guo et al. (2017) and Chen et al. (2020) investigated the fracture spacing and through-going fracture in layered rocks and the grain-scale failure of porous sandstone by the finite-discrete element method, respectively. Guo et al. (2020) developed a generic computational model for solving three-dimensional fragmentation problems of quasi-brittle materials. Tang et al. (2015) proposed the discontinuous deformation and displacement (DDD) method by combining the rock failure process analysis (RFPA) and the discontinuous deformation analysis (DDA). Using this method, Gong and Tang (2016) successfully reproduced the gradual slope sliding that occurred at the Alpetto Mine in Italy. In the DDD method, the complete model consists of an RFPA domain and a DDA domain. The RFPA module calculates crack creation and propagation, which can result in large displacements of elements. The elements that satisfy the large-displacement criterion are treated as DDA blocks automatically,

allowing for contact and separation between adjacent elements. However, this method has definite boundaries between the RFPA domain and the DDA domain, which limits its applicability. Gong et al. (2018) used the DDD method with the gravity increase method to investigate the recession process of notched rocky cliffs. Gong et al. (2019) further developed the DDD method to model the mechanical behaviors of joints within highly jointed rock masses. Nonetheless, for modeling the cross-scale failure process of discontinuous rock masses, to develop an effective solving algorithm that involves global equilibrium equation assembly, topology update, contact loop search, and other factors, is still challenging.

This study proposed a novel continuous to discontinuous method to analyze the cross-scale failure process of discontinuous rock masses, which includes the fine fracture creation, propagation, and penetration. To improve the stability and convergence, an implicit solving sequence was established. Furthermore, the assembly of contact matrices between adjacent subdomains into the global stiffness and loading matrices has been realized, and the mechanical contacts along the newly formed cracks can be characterized. Besides, structural surfaces with a certain thickness and without thickness can be simulated simultaneously. Then, the numerical tests were conducted to verify the correctness and validity of the proposed method in representing structural planes, describing nonlinear mechanical responses, and reproducing mesoscopic fracture propagation leading to rock failure. Additionally, the proposed method was applied to investigate the progressive failure process of a slope caused by gravity growth, providing insights into failure surfaces, deformation features, and instability mechanisms.

2. Methodology

2.1. The model and solution procedure

In the proposed model, the rock mass is capable of fracturing or crushing. Under external loading, when the Mohr-Coulomb strength criterion is reached with a tensile cut-off, new cracks are initiated and propagate within the rock. With an increase in load, the rock can be fragmented into smaller pieces due to the coalescence of new cracks. These fragments have contactable boundaries where opening, sliding, and interlocking can occur because vertex-vertex contact, vertex-edge contact, and edge-edge contact can be calculated, as depicted in Fig. 1. In the program, new nodes are added, and the new contact loops are updated after element failure and fracturing occurs.

At the start of the solution procedure, the rock mass model needs to be discretized into mesoscopic representative volume elements (RVEs). The strain and stress fields will then be calculated, and the fracture module will be used to control crack initiation and propagation based on the modified Mohr-Coulomb criterion with a tensile cutoff. If new element failure occurs, the program will search for new contact loops, and potential contacts can only occur between these loops. The edges of the failure elements will be transformed into newly generated contact interfaces, along which block detachment, slippage, friction, and locking can occur. The Newton's law of motion and contact theory (Shi, 2015) will be used to analyze the dynamic motion and block interactions of the rock mass. The contact force between two adjacent fragments will act at the related contact point. When a fragment moves, the other fragments around it will move accordingly due to their interactions. This means that the change in local deformation/movement will rapidly spread throughout the entire system. The dynamic equilibrium of the system can be achieved automatically by solving the local equilibrium equation with the coupled algorithm in each time step. This process will be repeated until the maximum calculation number is reached.

2.2. Assembly of equilibrium equations

This section aims to explain how the potential energy generated by various forces, stresses, and strains can affect the global stiffness and

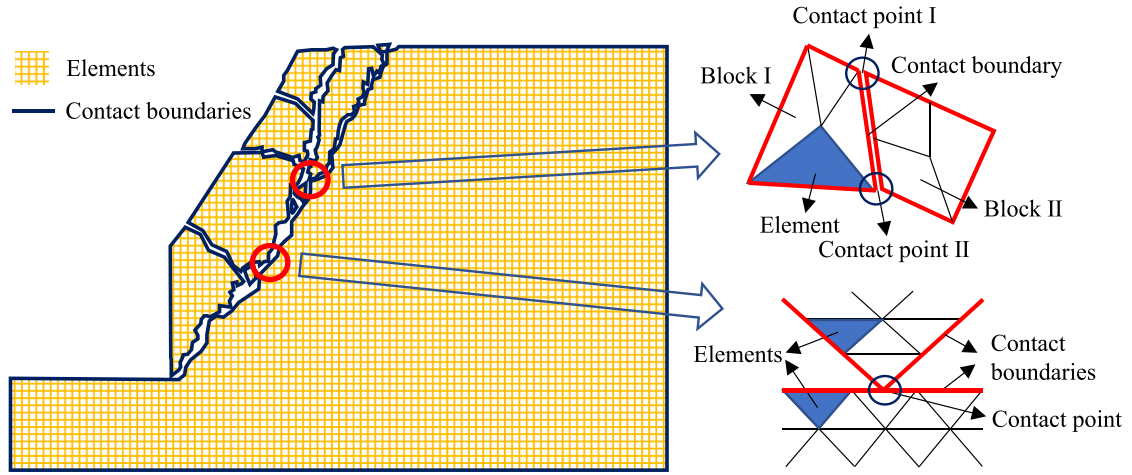


Fig. 1. Schematic diagram of the proposed model.

loading matrices in each calculation step, particularly in the assembly process of the global equilibrium equation. As an example, the assembly process of the global stiffness matrix will be discussed, and the load matrix can be assembled in a similar manner based on the specific mapping relationship of each submatrix.

Fig. 2 illustrates a mesh system composed of three blocks, each consisting of two or three triangular mesh elements. The interactions between the blocks occur through three pairs of contacts: edge-to-edge contact between Blocks 1 (B1) and 2 (B2), vertex-to-edge contact between Block 1 (B1) and 3 (B3), and vertex-to-edge contact between Block 2 (B2) and 3 (B3). To obtain the stiffness submatrices of the inner elements for each block (B1, B2, and B3), the potential energy of all submatrices except for contact forces is minimized. The corresponding stiffness submatrices are then added to obtain the stiffness submatrices of the three blocks (termed ‘Block-sum’), as depicted in Fig. 3. The total block stiffness matrix is obtained by assembling the three block stiffness submatrices. To consider mechanical contacts, the contact stiffness submatrices are calculated by minimizing the potential energy caused by normal spring, tangential spring, or friction, as illustrated in Fig. 4. The total contact stiffness matrix (termed ‘Contact-sum’) is obtained by adding up the three contact stiffness submatrices. The global stiffness matrix is obtained by adding up the total block and contact stiffness

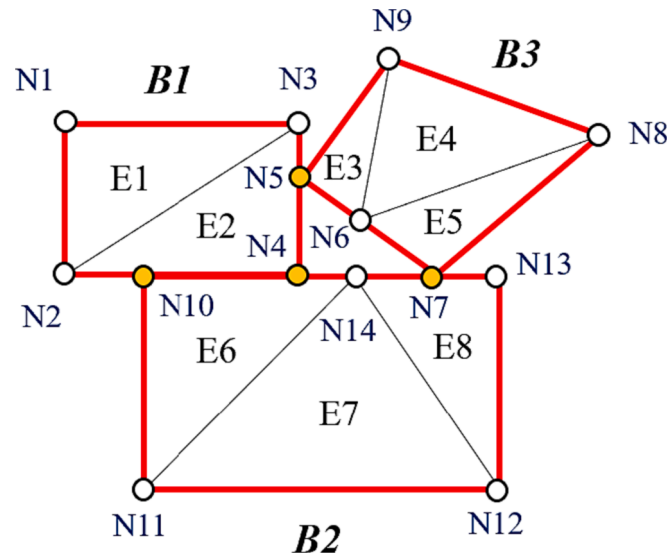


Fig. 2. The numerical framework of three blocks in contact in the proposed model.

matrices, as also shown in Fig. 4. The darker color in Figs. 3 and 4 indicates the higher frequency of the corresponding matrix element being updated during the assembly process of the global stiffness matrix. It is worth noting that since the block system may generate some sub-potential energy, all potential energy items, except for contact forces, are considered as a whole and recorded once, as shown in Fig. 3. Additionally, the dimension of the global stiffness matrix may vary in different calculation steps due to the possibility of generating new joint interfaces.

2.3. Displacement function

In the proposed method, triangular elements are used as the solution targets, and the basic unknown variables are the displacement components of element nodes. Consider a triangular element E_m with three nodes, i, j , and k , numbered in a counterclockwise order. The displacement of any point (x, y) within the element can be uniquely determined by the six displacement components of the three nodes, as:

$$\begin{cases} u = (f_i(x, y) & f_j(x, y) & f_k(x, y)) \begin{Bmatrix} u_i \\ u_j \\ u_k \end{Bmatrix} \\ v = (f_i(x, y) & f_j(x, y) & f_k(x, y)) \begin{Bmatrix} v_i \\ v_j \\ v_k \end{Bmatrix} \end{cases} \quad (1)$$

where the displacement components of the three nodes along the x -axis and y -axis are (u_i, v_i) , (u_j, v_j) and (u_k, v_k) , respectively.

The force–displacement relationship can be expressed as:

$$\begin{cases} f_i(x, y) \\ f_j(x, y) \\ f_k(x, y) \end{cases} = \frac{1}{\begin{vmatrix} 1 & x_i & y_i \\ 1 & x_j & y_j \\ 1 & x_k & y_k \end{vmatrix}} \begin{bmatrix} x_j y_k - x_k y_j & x_k y_i - x_i y_k & x_i y_j - x_j y_i \\ y_j - y_k & y_k - y_i & y_i - y_j \\ x_k - x_j & x_i - x_k & x_j - x_i \end{bmatrix} \begin{Bmatrix} 1 \\ x \\ y \end{Bmatrix} \quad (2)$$

where the coordinates of the three nodes along the x -axis and y -axis are (x_i, y_i) , (x_j, y_j) and (x_k, y_k) , respectively.

2.4. Global equilibrium equation

To begin with, the potential energy equations arising from various forces and stresses, such as strain potential energy, initial stress potential energy, point load potential energy, volume load potential energy,

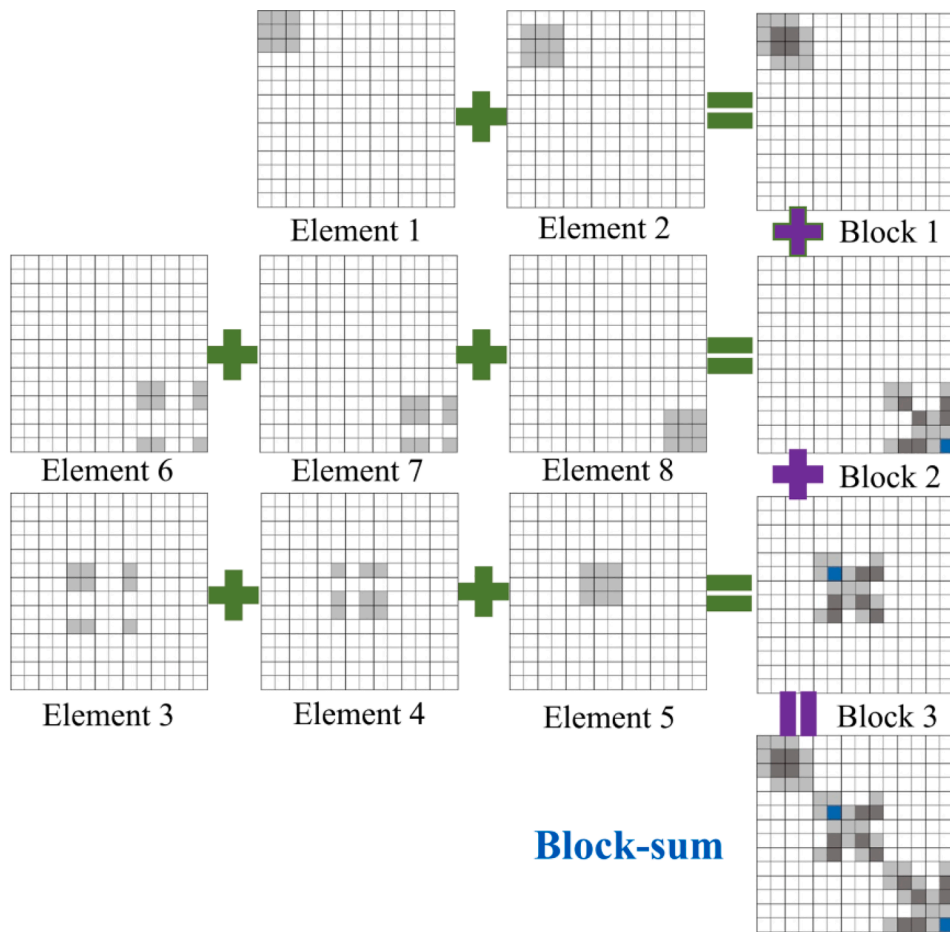


Fig. 3. Assembly of block stiffness matrix.

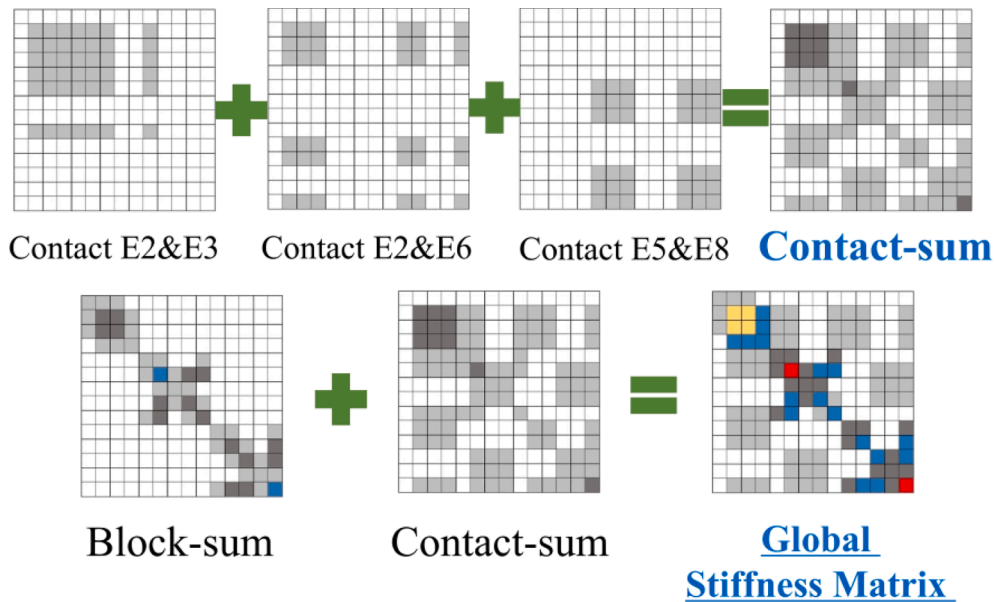


Fig. 4. Assembly of contact matrix and global stiffness matrix.

inertia force potential energy, contact spring strain potential energy, and friction potential energy, are compiled. Next, the partial derivative equations for each potential energy component along the x-axis and y-axis are computed. The resulting sub matrices are then added to their respective positions in the global equilibrium equation. Furthermore, at

each time step, the changes in each potential energy component can be updated to achieve automatic equilibrium of the system.

The element stiffness matrix is defined over the integral domain where the element is located. Let S^m be the area of the element E_m . The element stiffness matrix can then be expressed as follows:

$$K_e^m = S^m \begin{Bmatrix} B_i^T \\ B_j^T \\ B_k^T \end{Bmatrix} D [B_i \ B_j \ B_k] \quad (3)$$

where D represents the element elastic matrix, which is a combination of elastic modulus and Poisson's ratio in isotropic plane stress or plane strain problems. The matrix $[B_i \ B_j \ B_k]$ is expressed as:

$$[B_i \ B_j \ B_k] = \begin{bmatrix} \frac{\partial f_i(x,y)}{\partial x} & 0 & \frac{\partial f_j(x,y)}{\partial x} & 0 & \frac{\partial f_k(x,y)}{\partial x} & 0 \\ 0 & \frac{\partial f_i(x,y)}{\partial y} & 0 & \frac{\partial f_j(x,y)}{\partial y} & 0 & \frac{\partial f_k(x,y)}{\partial y} \\ \frac{\partial f_i(x,y)}{\partial y} & \frac{\partial f_i(x,y)}{\partial x} & \frac{\partial f_j(x,y)}{\partial y} & \frac{\partial f_j(x,y)}{\partial x} & \frac{\partial f_k(x,y)}{\partial y} & \frac{\partial f_k(x,y)}{\partial x} \end{bmatrix} \quad (4)$$

To compute the initial stress matrix in the proposed method, the potential energy generated by the updated initial stress must be calculated. This is because the method employs a step-by-step solving approach, where the stress computed in the previous step is used as the initial stress for the current step. The matrix can be expressed as follows:

$$F_\sigma^m = -S^m B^T \sigma_m^0 = -S^m \begin{Bmatrix} B_i^T \\ B_j^T \\ B_k^T \end{Bmatrix} \begin{Bmatrix} \sigma_x^0 \\ \sigma_y^0 \\ \tau_{xy}^0 \end{Bmatrix} \quad (5)$$

where the initial stresses along the x -direction, y -direction, and the shear stress in the plane coordinate system are denoted as σ_x^0 , σ_y^0 and τ_{xy}^0 , respectively.

In the proposed model, the point load matrix differs from the traditional finite element method in that load points can be any point inside elements, not only element nodes. For instance, if a load point acts on the point (x_0, y_0) inside the element E_m , with p_x and p_y being the two components of the point load along the x -axis and y -axis, respectively, the corresponding matrix can be expressed as follows:

$$F_p^m = \begin{Bmatrix} [N_i(x_0, y_0)]^T \\ [N_j(x_0, y_0)]^T \\ [N_k(x_0, y_0)]^T \end{Bmatrix} \begin{Bmatrix} p_x \\ p_y \end{Bmatrix} \quad (6)$$

with

$$(N_i(x,y) \ N_j(x,y) \ N_k(x,y)) = \begin{bmatrix} f_i(x,y) & 0 & f_i(x,y) & 0 & f_i(x,y) & 0 \\ 0 & f_i(x,y) & 0 & f_i(x,y) & 0 & f_i(x,y) \end{bmatrix} \quad (7)$$

In the displacement constraint matrix, all constraint points are imposed on the corresponding element nodes as boundary conditions, and their movements are restricted by two rigid springs. If the constraint point (x_0, y_0) is located inside the element E_m , the displacement constraint matrix can be expressed as follows:

$$K_c^m = k \begin{Bmatrix} [N_i(x_0, y_0)]^T \\ [N_j(x_0, y_0)]^T \\ [N_k(x_0, y_0)]^T \end{Bmatrix} (N_i(x_0, y_0) \ N_j(x_0, y_0) \ N_k(x_0, y_0)) \quad (8)$$

where k is the stiffness of two rigid springs along the x and y directions at the constraint point.

For the body load matrix, it can be expressed as follows:

$$F_b^m = \iint_A \begin{Bmatrix} [N_i(x_0, y_0)]^T \\ [N_j(x_0, y_0)]^T \\ [N_k(x_0, y_0)]^T \end{Bmatrix} dx dy \begin{Bmatrix} f_x \\ f_y \end{Bmatrix} \quad (9)$$

where the operator ' \iint_A ' represents the double integral over the area A of

the element E_m ; f_x, f_y are the volume forces per unit area acting on the element E_m .

In dynamic calculations, the inertia force matrix needs to be considered. In the proposed method, this matrix is analogous to the mass matrix in finite element analysis and plays a significant role in maintaining the overall balance of the model in each time step. The inertia force matrix for the current time step can be expressed as follows:

$$K_m^m = \frac{4M}{\Delta t^2} \iint_A \begin{Bmatrix} [N_i(x,y)]^T \\ [N_j(x,y)]^T \\ [N_k(x,y)]^T \end{Bmatrix} (N_i(x,y) \ N_j(x,y) \ N_k(x,y)) dx dy \quad (10)$$

where Δt is the time step, and M is the mass per unit material area.

2.5. Block contact matrix

To improve the deformability of a single block and refine the stress distribution within it, the proposed program embeds multiple elements into the model block, allowing it to be broken down into smaller blocks during the calculation. Elements that meet the strength criteria are treated as failure elements, and their edges form new joints, enabling opening, sliding, and locking between elements. Contact processing in the proposed method only involves boundary loops that comprise joints. In the 2D coordinate system, three types of contacts need to be considered, namely node-to-node, node-to-edge, and edge-to-edge contacts. When the contact search algorithm detects an existing contact point, it calculates the normal and tangential intrusion distances at that point. The normal spring, tangential spring, or friction is then added at this point, and the corresponding stiffness matrices are included in the global equilibrium equation. Clearly, P_1 is the vertex belonging to the element E_m ; P_2P_3 is the entry edge belonging to the element E_n with a length of l . The points P_1, P_2, P_3 are sequentially named in the counter-clockwise direction from the positive x -axis direction to the positive y -axis direction. The coordinates of point P_k ($k = 1, 2, 3$) are defined as (x_k, y_k) . k_n is the normal spring stiffness. The normal stiffness matrices can be expressed as follows:

$$K_{kn}^{mm} = k_n \begin{Bmatrix} H_{m(1)} \\ H_{m(2)} \\ H_{m(3)} \end{Bmatrix} (H_{m(1)}^T \ H_{m(2)}^T \ H_{m(3)}^T) \quad (11)$$

$$K_{kn}^{mm} = k_n \begin{Bmatrix} H_{m(1)} \\ H_{m(2)} \\ H_{m(3)} \end{Bmatrix} (G_{n(1)}^T \ G_{n(2)}^T \ G_{n(3)}^T) \quad (12)$$

$$K_{kn}^{mm} = k_n \begin{Bmatrix} G_{n(1)} \\ G_{n(2)} \\ G_{n(3)} \end{Bmatrix} (H_{m(1)}^T \ H_{m(2)}^T \ H_{m(3)}^T) \quad (13)$$

$$K_{kn}^{mm} = k_n \begin{Bmatrix} G_{n(1)} \\ G_{n(2)} \\ G_{n(3)} \end{Bmatrix} (G_{n(1)}^T \ G_{n(2)}^T \ G_{n(3)}^T) \quad (14)$$

where

$$\begin{Bmatrix} H_{m(1)} \\ H_{m(2)} \\ H_{m(3)} \end{Bmatrix} = \frac{1}{l} \begin{Bmatrix} [N_{m(1)}(x_1, y_1)]^T \\ [N_{m(2)}(x_1, y_1)]^T \\ [N_{m(3)}(x_1, y_1)]^T \end{Bmatrix}^T \begin{Bmatrix} y_2 - y_3 \\ x_3 - x_2 \end{Bmatrix} \quad (15)$$

$$\begin{Bmatrix} G_{n(1)} \\ G_{n(2)} \\ G_{n(3)} \end{Bmatrix} = \frac{1}{l} \begin{Bmatrix} [N_{n(1)}(x_2, y_2)]^T \\ [N_{n(2)}(x_2, y_2)]^T \\ [N_{n(3)}(x_2, y_2)]^T \end{Bmatrix}^T \begin{Bmatrix} y_3 - y_1 \\ x_1 - x_3 \end{Bmatrix} + \frac{1}{l} \begin{Bmatrix} [N_{n(1)}(x_3, y_3)]^T \\ [N_{n(2)}(x_3, y_3)]^T \\ [N_{n(3)}(x_3, y_3)]^T \end{Bmatrix}^T \begin{Bmatrix} y_1 - y_2 \\ x_2 - x_1 \end{Bmatrix} \quad (16)$$

Simultaneously, the corresponding load matrices can be expressed as:

$$F_{kn}^m = -k_n \frac{S_0}{l} H = -k_n \frac{S_0}{l} \begin{Bmatrix} H_{m(1)} \\ H_{m(2)} \\ H_{m(3)} \end{Bmatrix} \quad (17)$$

$$F_{kn}^n = -k_n \frac{S_0}{l} G = -k_n \frac{S_0}{l} \begin{Bmatrix} G_{n(1)} \\ G_{n(2)} \\ G_{n(3)} \end{Bmatrix} \quad (18)$$

where

$$S_0 = \begin{bmatrix} 1 & x_1 & y_1 \\ 1 & x_2 & y_2 \\ 1 & x_3 & y_3 \end{bmatrix} \quad (19)$$

In the tangential direction, the tangential spring will be added along $\vec{P_2P_3}$ at P_0 . Let k_t be the tangential spring stiffness, the spring stiffness matrices can be expressed as follows:

$$K_{kt}^{mm} = k_t H H^T = \begin{Bmatrix} H_{m(1)} \\ H_{m(2)} \\ H_{m(3)} \end{Bmatrix} \begin{pmatrix} H_{m(1)}^T & H_{m(2)}^T & H_{m(3)}^T \end{pmatrix} \quad (20)$$

$$K_{kt}^{mn} = k_t H G^T = \begin{Bmatrix} H_{m(1)} \\ H_{m(2)} \\ H_{m(3)} \end{Bmatrix} \begin{pmatrix} G_{n(1)}^T & G_{n(2)}^T & G_{n(3)}^T \end{pmatrix} \quad (21)$$

$$K_{kt}^{nn} = k_t G H^T = \begin{Bmatrix} G_{n(1)} \\ G_{n(2)} \\ G_{n(3)} \end{Bmatrix} \begin{pmatrix} H_{m(1)}^T & H_{m(2)}^T & H_{m(3)}^T \end{pmatrix} \quad (22)$$

$$K_{kt}^{nn} = k_t G G^T = \begin{Bmatrix} G_{n(1)} \\ G_{n(2)} \\ G_{n(3)} \end{Bmatrix} \begin{pmatrix} G_{n(1)}^T & G_{n(2)}^T & G_{n(3)}^T \end{pmatrix} \quad (23)$$

Simultaneously, the corresponding load matrices can be expressed as follows:

$$F_{kt}^m = -k_t \frac{S_0}{l} H = -k_t \frac{S_0}{l} \begin{Bmatrix} H_{m(1)} \\ H_{m(2)} \\ H_{m(3)} \end{Bmatrix} \quad (24)$$

$$F_{kt}^n = -k_t \frac{S_0}{l} G = -k_t \frac{S_0}{l} \begin{Bmatrix} G_{n(1)} \\ G_{n(2)} \\ G_{n(3)} \end{Bmatrix} \quad (25)$$

In the proposed method, sliding occurs at a contact point when Coulomb's law of friction is satisfied at the discontinuous interface. To account for physical friction along the sliding interface, the friction-induced potential energy must be considered. Specifically, when the point P_1 , which belongs to element E_m , enters the edge P_2P_3 belonging to element E_n at entry point P_0 , the magnitude of the friction force can be calculated based on the normal pressure, while the direction of the friction force can be determined by projecting P_1P_0 along the vector $\vec{P_2P_3}$. Then, the load matrix caused by the friction F at P_1 on the element E_m can be described as:

$$F_f^m = -FH = -F \begin{Bmatrix} H_{m(1)} \\ H_{m(2)} \\ H_{m(3)} \end{Bmatrix} \quad (26)$$

Meanwhile, the load matrix caused by the friction F at P_0 on the element E_n can be described as:

$$F_f^n = FG = F \begin{Bmatrix} G_{n(1)} \\ G_{n(2)} \\ G_{n(3)} \end{Bmatrix} \quad (27)$$

To prevent block overlapping or embedding, a penalty function method is used in the proposed program. To ensure that each contact point maintains a state of no tension and no embedment throughout the calculation process, an open-close iteration (Doolin and Sitar, 2002) is

incorporated into the program. Some researchers have recommended setting the penalty spring stiffness to 10–1000 times greater than the elastic modulus (Shi, 1988). However, setting a high penalty spring stiffness can lead to an ill-conditioned global stiffness matrix, which can adversely affect solution convergence. Therefore, the current program employs a soft contact process (Cheng, 1998) that allows some degree of mutual embedding. This approach is consistent with field observations where chisel marks are frequently observed at rock interfaces.

The above explanations provide a detailed account of the theoretical formulas employed in the proposed method. Firstly, the element displacement function is introduced, with node displacements of triangular elements serving as the fundamental unknowns. Next, the global equilibrium equation is obtained by assembling all the element stiffness/load matrices. To ensure that all potential energy contributions are accounted for in the simulation, element submatrices caused by different forces, strains, and stresses can be calculated by minimizing the corresponding potential energy. In addition, submatrices induced by normal spring, tangential spring, and friction are derived to reflect the mechanical contact between adjacent blocks. These formulas form the theoretical basis for the implementation of the program. Notably, as a whole-process analysis method, the proposed method incorporates both the displacement function and the control equation as well as the relevant kinematics and contact theory. The code has been written in the C programming language.

2.6. Block fracturing process

Two main steps are involved in generating new cracks in the proposed method: (1) separating the element edges and common nodes of the elements that meet the strength criteria from the adjacent elements. This means that when a grid line becomes a joint, the adjacent elements on both sides of it are separated, and new nodes are added; (2) updating the contact boundaries in the new mesh. Since the search for contact boundaries needs to be performed in every calculation step, a valid contact searching algorithm is essential for the computational efficiency of the method.

To ensure the high efficiency of the proposed program, a simple and fast searching algorithm has been developed. For better understanding, the basic terms are defined: (1) Internal node: the nodes located inside the model block; (2) External node: the nodes located at the boundaries of the model block; (3) Contact loop: the directional joint circuits inside or along the boundaries of the model block; (4) Loop search direction: when moving along a circuit, if the material wrapped by the circuit is always on the left-hand side of the travel direction, this direction is termed the loop search direction, as shown in Fig. 5; (5) Upper node: for an external node, the first node encountered along the loop search direction of a contact loop; (6) Lower node: for an external node, the first node encountered along the opposite loop search direction of a contact loop.

The contact searching loop is illustrated in Fig. 6. Since all contact loops are composed of external nodes, the first step is to identify all external nodes in the model prior to calculation. Then, the searching process can commence along the loop search direction from any unused external node. For the current node, if the number of its upper node matches the number of the starting node of the current search, the search will terminate, and the sequence number of the involved external nodes of this loop will be stored. If not, the current node will be replaced by its upper node until the loop is closed.

3. Numerical implementations

3.1. The stress–strain relationship and strength criterion

Drawing on the statistical damage theory (Liang, 2005), the linear elastic constitutive relationship of each element holds until failure. Once the threshold stress is reached, the failed element will follow a strain-

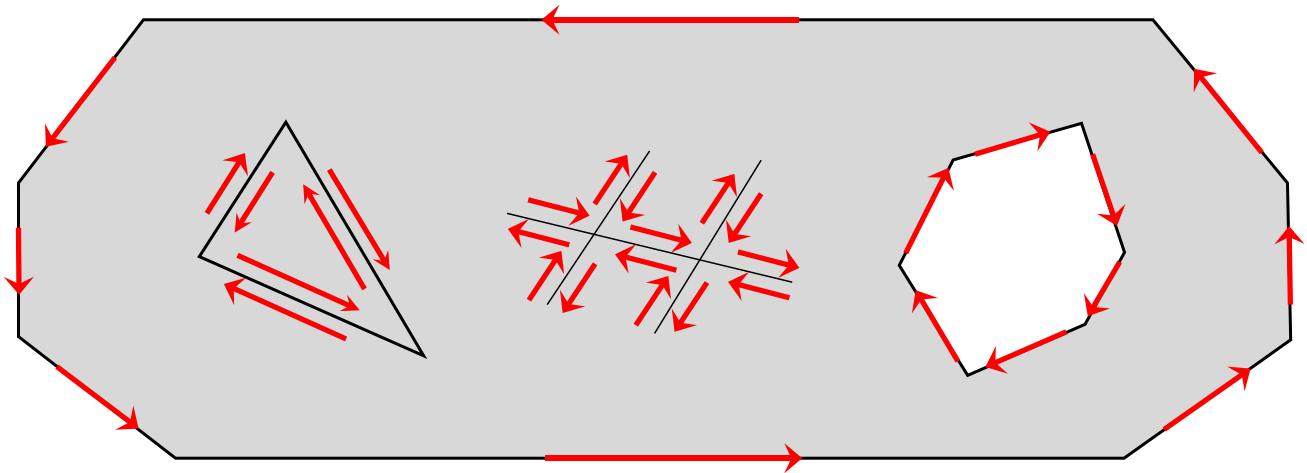


Fig. 5. An illustration of contact searching loop.

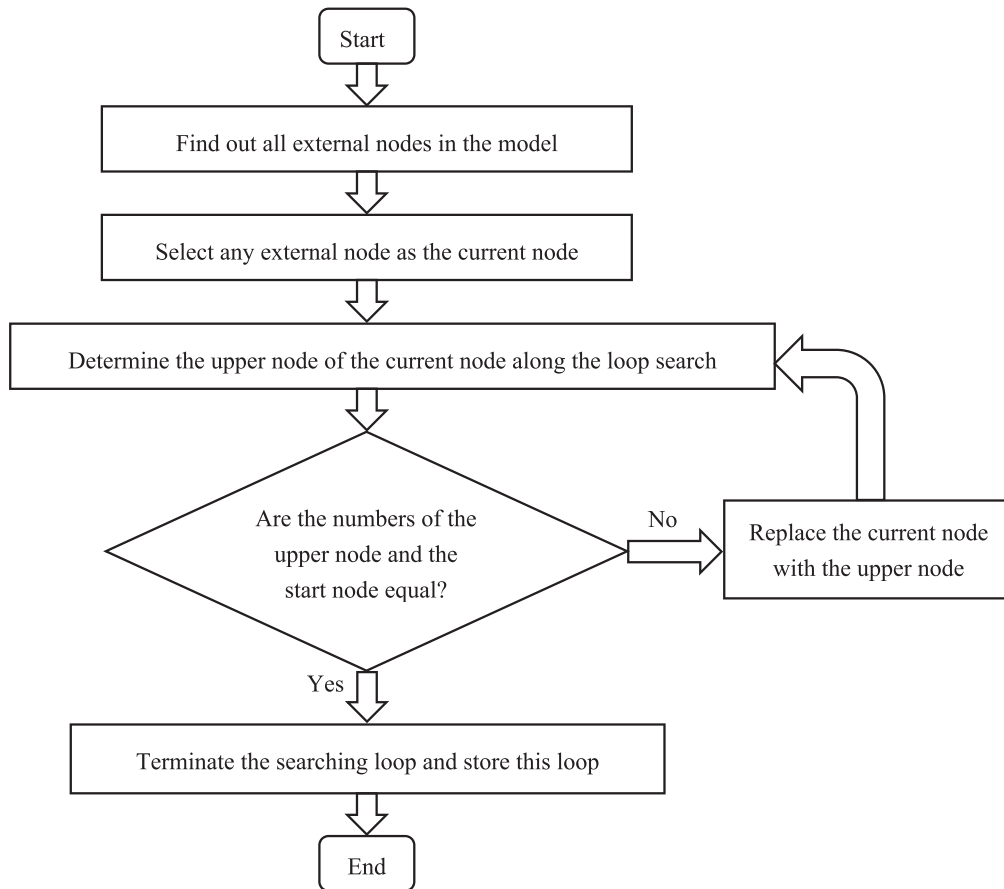


Fig. 6. Contact loop search scheme.

softening relationship in accordance with the strength criterion as shown in Fig. 7. Although the constitutive relationship of Representative Volume Elements (RVEs) is linear elasto-brittle-plastic, the macroscopic mechanical behavior of the entire model can be intricate due to the non-uniform distribution of input parameters.

In the modelling, the elastic modulus of each damaged element will be systematically weakened in proportion to the intensity of damage, as follows:

$$E = (1 - \omega)E_0 \tag{28}$$

where ω is the damage index; E and E_0 are the elastic moduli of an element at the damaged state and initial state, respectively. It should be noted that in this study, the simulated finite elements and the damage are considered to be isotropic (Tang et al., 2002).

Under tension (see the curves in the third quadrant of Fig. 7), the damage index ω is defined as:

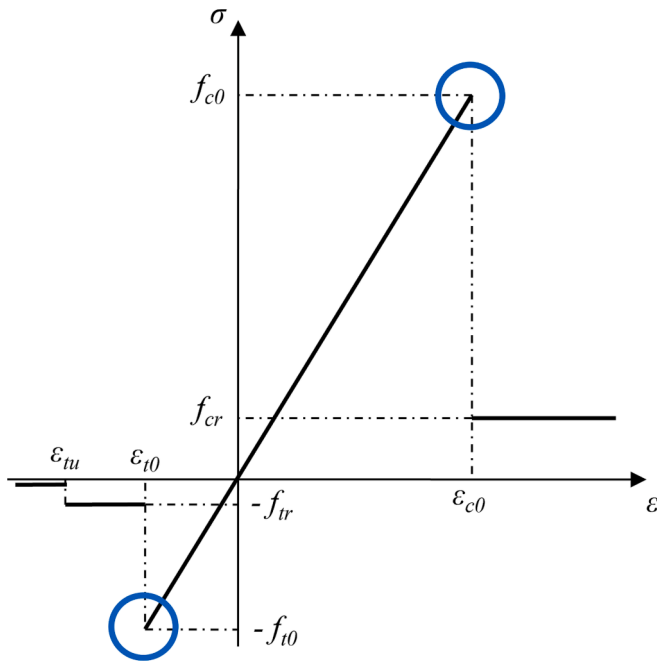


Fig. 7. The constitutive stress-strain relationship of elements under uniaxial compression or tension loading.

$$\omega = \begin{cases} 0 & \varepsilon > \varepsilon_{t0} \\ 1 - \frac{\lambda \varepsilon_{t0}}{\varepsilon} & \varepsilon_{lu} < \varepsilon \leq \varepsilon_{t0} \\ 1 & \varepsilon \leq \varepsilon_{lu} \end{cases} \quad (29)$$

where λ is the residual strength coefficient, which is defined as $\lambda = f_{lr}/f_{t0} = f_{lr}/(E_0\varepsilon_{t0})$; f_{t0} and f_{lr} are the uniaxial peak and residual tensile strengths, respectively; ε_{t0} is the threshold tensile strain at the elastic limit state; ε_{lu} is the ultimate tensile strain at failure.

Under compression (see the curves in the first quadrant of Fig. 7), shear damage will appear if the stress state of the element meets the compression-shear strength criterion. The damage variable ω is defined as:

$$\omega = \begin{cases} 0 & \varepsilon < \varepsilon_{c0} \\ 1 - \frac{\lambda \varepsilon_{c0}}{\varepsilon} & \varepsilon \geq \varepsilon_{c0} \end{cases} \quad (30)$$

where λ is defined as $\lambda = f_{cr}/f_{c0} = f_{cr}/(E_0\varepsilon_{c0})$; f_{c0} and f_{cr} are the uniaxial peak and residual compressive strengths, respectively; ε_{c0} is the threshold compressive strain.

When an element is subjected to a multiaxial stress state and meets the compression-shear strength criterion, shear damage will also occur. To account for the influence of multiaxial stresses, the threshold compressive strain ε_{c0} can be calculated as follows, based on the work of Tang et al. (2002).

$$\varepsilon_{c0} = \frac{1}{E_0} \left[f_{c0} + \frac{1 + \sin\varphi}{1 - \sin\varphi} \sigma_3 - \mu(\sigma_1 + \sigma_2) \right] \quad (31)$$

where φ is the internal friction angle; μ is the Poisson's ratio; σ_1 , σ_2 and σ_3 are the maximum, intermediate and minimum principal stresses, respectively.

The studies conducted by Hoxha and Homand (2000) and Meglis et al. (1995) suggest that the process of rock fracturing involves the coupling of various failure modes, such as tensile failure, compression-shear failure, crack opening, and crack slipping. To describe this coupling process, the modified Mohr-Coulomb strength criterion with a tensile cut-off was adopted, as shown in Fig. 8.

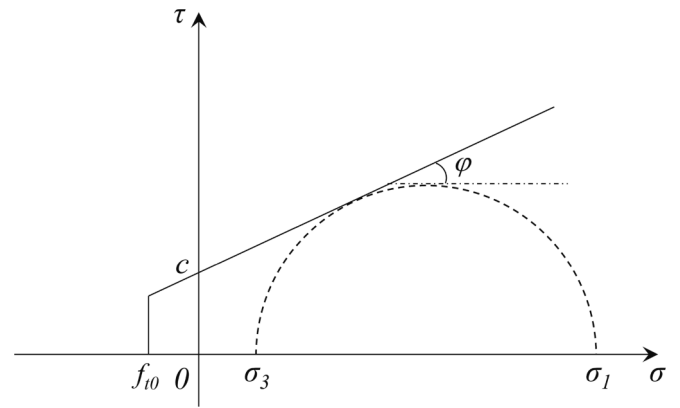


Fig. 8. The Mohr-Coulomb strength criterion with a tensile cut-off.

In this approach, an element will be considered to have failed if either the Mohr-Coulomb criterion or the maximum tensile stress criterion is satisfied, as follows:

Mohr-Coulomb strength criterion:

$$\tau \geq c + \sigma \tan\varphi \text{ or } f_{c0} \leq \sigma_1 - \frac{1 + \sin\varphi}{1 - \sin\varphi} \sigma_3 \quad (32)$$

where τ and σ are the shear and normal stresses, respectively; c is the cohesion.

Maximum tensile stress criterion:

$$\sigma_3 \leq f_{t0} \quad (33)$$

3.2. Statistical distribution of material parameters

The heterogeneity of material properties is a significant characteristic of rock masses that can greatly influence their nonlinear deformation and progressive failure (Manthei, 2005). To account for the influence of mesoscopic rock heterogeneity on complex macroscopic behaviors, the material parameters of RVEs within the model can be assumed to follow a given statistical distribution function based on statistical strength theory. The Weibull distribution has been widely used by researchers to describe the probabilistic distribution of rock material parameters (Weibull, 1951; Basu et al., 2009; Sanchidrian et al., 2014; Fu et al., 2017; Nassar et al., 2018). This distribution can be expressed as:

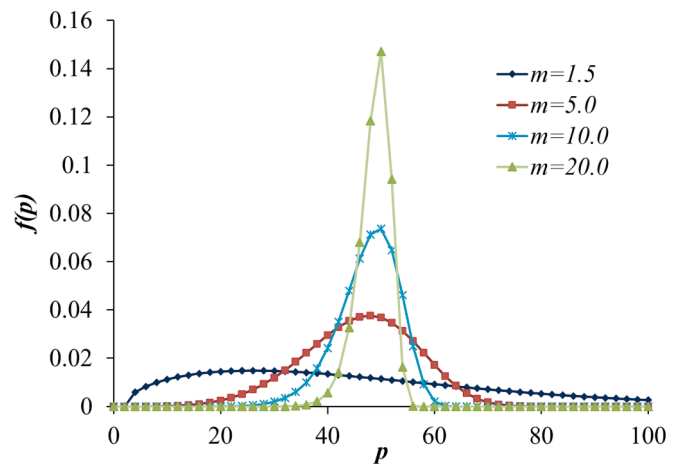


Fig. 9. Weibull distribution of material properties under different homogeneity coefficients.

$$f(p) = \frac{m}{p_0} \left(\frac{p}{p_0}\right)^{m-1} \exp\left(-\left(\frac{p}{p_0}\right)^m\right) \quad (34)$$

where p represents a specific mechanical property of mesoscopic elements, such as elastic modulus, cohesion, or strength; p_0 is the mean value of the parameter p ; m (where $m > 1$) is the homogeneity coefficient that reflects the shape of the probability density function. The distribution densities of the mechanical parameter p under different homogeneity coefficients m are depicted in Fig. 9.

Based on a given probability density function, a non-uniform model consisting of multiple RVEs can be created numerically using the Monte Carlo method. As illustrated in Fig. 10, for an average elastic modulus of 50 GPa, four representative numerical samples with homogeneity coefficients “ m ” of 1.5, 5, 10, and 20 are generated according to the Weibull distribution. It can be observed from Fig. 10 that as the homogeneity coefficient “ m ” decreases, the elastic modulus of each element shows significant variability. However, as “ m ” increases, the distribution of elastic moduli tends to become more uniform. When “ m ” reaches 100, the sample becomes nearly uniform, with all elements having elastic modulus values close to 50 GPa. Fig. 11 reveals that the overall macroscopic mechanical behavior of the inhomogeneous rock sample can be complex due to the non-uniform distribution of material parameters, even though the constitutive relationship of RVEs is linear elasto-brittle-plastic.

4. Model calibration and application

In this section, the proposed method in this study was calibrated by simulating uniaxial compression and direct shear tests of rock mass. Subsequently, the calibrated method was utilized to investigate the evolution of slope failure and mass movement, as well as the formation of slope failure surfaces.

4.1. Modelling of uniaxial compression test

To validate the performance of the proposed method in simulating the initiation, propagation, and nucleation of rock cracks, a numerical rock sample with dimensions of 150 mm in height and 75 mm in diameter was subjected to uniaxial compression loading. The physical and mechanical parameters, including elastic modulus, cohesion, and tensile strength, were assumed to follow a Weibull distribution with a homogeneity coefficient (m) of 1.5. The model was divided into 8,100 elements, with the bottom boundary fixed along the normal direction, and subjected to downward loading with a displacement-control rate of 0.02 mm/s. This loading rate can be considered quasi-static/static, and any dynamic effects can be ignored, as suggested by previous studies (Ha et al., 2015; Li and Wong, 2012). The details of the model and its parameters are provided in Table 1.

Fig. 12 illustrates the crack initiation and propagation processes

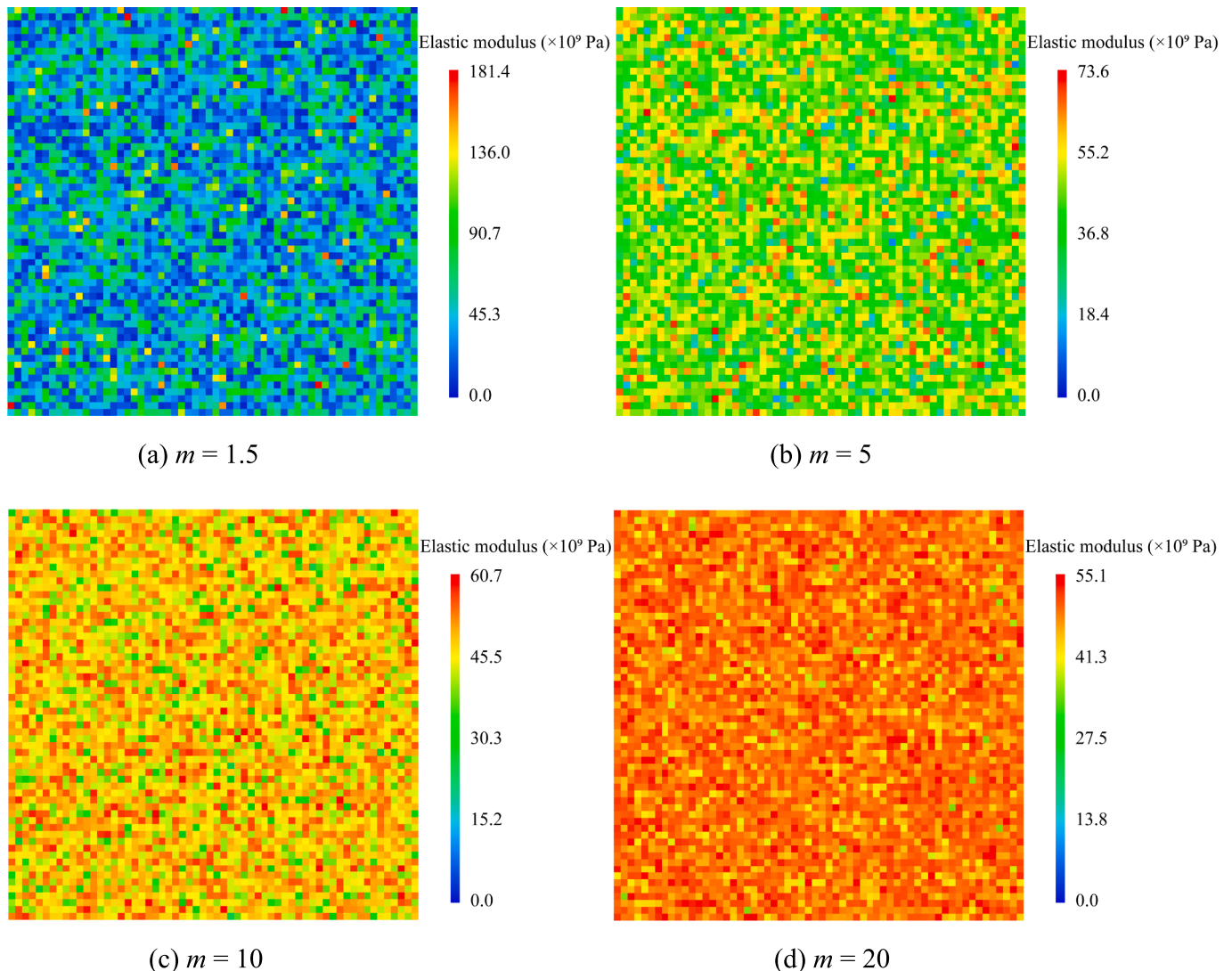


Fig. 10. Numerical samples with different homogeneity coefficients m (each sample contains 50×50 elements).

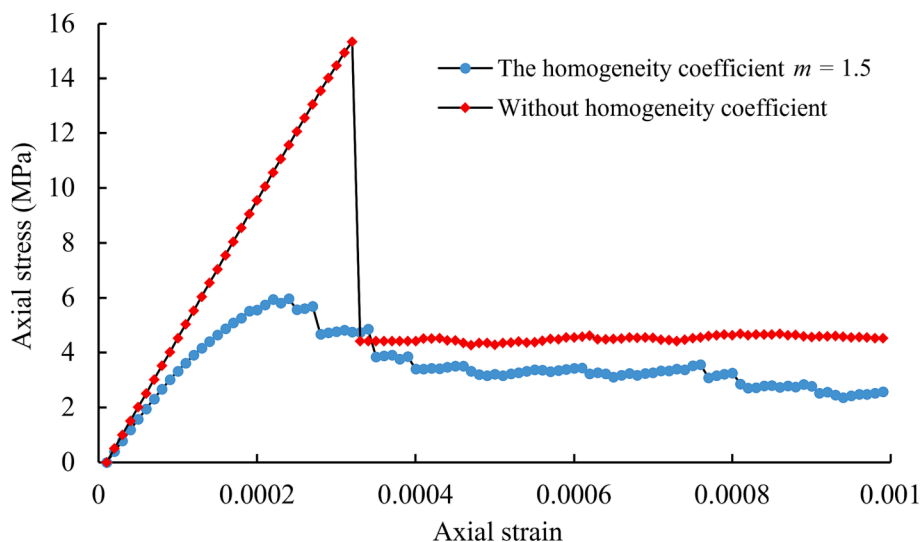


Fig. 11. Typical macroscopic stress–strain relationship for testing inhomogeneous rock.

observed during the uniaxial compression test. Initially, due to the non-uniform distribution of material properties, some finite elements in weak regions experienced damage, representing potential crack initiation locations and influencing subsequent crack propagation, as shown in Fig. 12 (a). Subsequently, as micro-cracks developed and nucleated within the sample, a longer crack located at the lower right side and a shorter one at the middle right side of the sample can be clearly observed in Fig. 12 (b). Notably, there were evident stress concentrations at the propagating front of these cracks, which promoted the continuous upward and downward development of the cracks. As the cracks evolved, the concentrated stresses were released and transferred to the new crack tips.

Fig. 12 (c) shows that as the load increased, the two initially independent cracks eventually connected with each other at the middle of the sample, forming a more complex crack distribution pattern. At the same time, due to the influence of material heterogeneity, the strength of mesh elements in some regions can be higher than that of the surrounding ones. This mechanism resulted in the formation of a small isolated rock block near the boundary at the lower right corner, where high stresses were observed. This phenomenon highlights an important advantage of the proposed model with the coupled solving algorithm, as it allows for deformable rock to be broken into fragments without making assumptions about where and how cracks are initiated and propagated. Furthermore, after the two main cracks nucleated, the newly formed crack continued to propagate towards the upper left corner, ultimately resulting in the separation of the original rectangular specimen into two large pieces, and the dip angle of the main failure surface is 54.61° as depicted in Fig. 12 (d). The numerical results obtained from the proposed method are consistent with the well-documented finite element method (RFPA) and discrete element method (DEM) models by Tang et al. (2000) and Shimizu et al. (2010), as shown in Fig. 12 (e) and (f).

Table 1
Physical-mechanical properties of the rock specimen for uniaxial compression.

Parameter	Value
Elastic modulus E (GPa)	50
Poisson's ratio ν	0.2
Homogeneity coefficient m	1.5
Cohesion c (MPa)	100
Internal friction angle φ ($^\circ$)	20
Uniaxial tensile strength f_{t0} (MPa)	7

4.2. Modelling of direct shear test

The rock properties under direct shear loading were analyzed using the proposed program and compared with experimental data. The 2D model had dimensions of $200 \text{ mm} \times 200 \text{ mm}$, as shown in Fig. 13 (a), and was divided into 55,162 elements.

The physical and mechanical parameters are listed in Table 2, among which the elastic modulus, cohesion, and tensile strength, were assumed to follow a Weibull distribution with a homogeneity coefficient (m) of 5. The left and bottom boundaries of the lower half of the model were fixed along the corresponding normal direction, while the top boundary was subjected to a normal stress σ_p , and the right boundary of the upper half of the model was horizontally loaded with a ratio of 0.0025 mm/s, as illustrated in Fig. 13. As the shear strain increased, cracks progressively developed within the rock sample. Initially, cracks were initiated at both sides of the model near the boundary between the upper and lower halves of the model, due to shear concentration and strain localization. It is evident that shear stress concentrated at the crack front, governing the occurrence and propagation direction of the cracks. Subsequently, micro-cracks propagated and nucleated to form several larger cracks in the middle. These cracks eventually became interconnected and split the rock sample into two major blocks.

At the failure state, the normal and shear stresses acting on the rock sample were recorded and analyzed. The shear strengths of the rock samples obtained from numerical and experimental tests for different normal loadings are summarized in Fig. 14. While some data scattering exists, the numerical results closely match the experimental data. The overall trend indicates that the shear strength increased with the normal stress, which is consistent with the principles of classic rock mechanics.

4.3. Model application in investigating progressive slope failure

The proposed method, which combines damage mechanics, contact mechanics, and kinematics, is well-suited for modeling slope failure processes that involve crack creation and growth at small deformation states, as well as block contact and collision at large displacement states. To investigate the failure characteristics of a landslide, a slope with a height of 25 m and a slope inclination of 2.5V:1H was configured, as shown in Fig. 15.

The material properties of the slope are listed in Table 3. The numerical model consisted of approximately 50,000 elements. The left side, right side, and bottom of the model were fixed along the corresponding normal direction, while the top was left free. The gravity of the slope was gradually increased step by step, and when the gravity

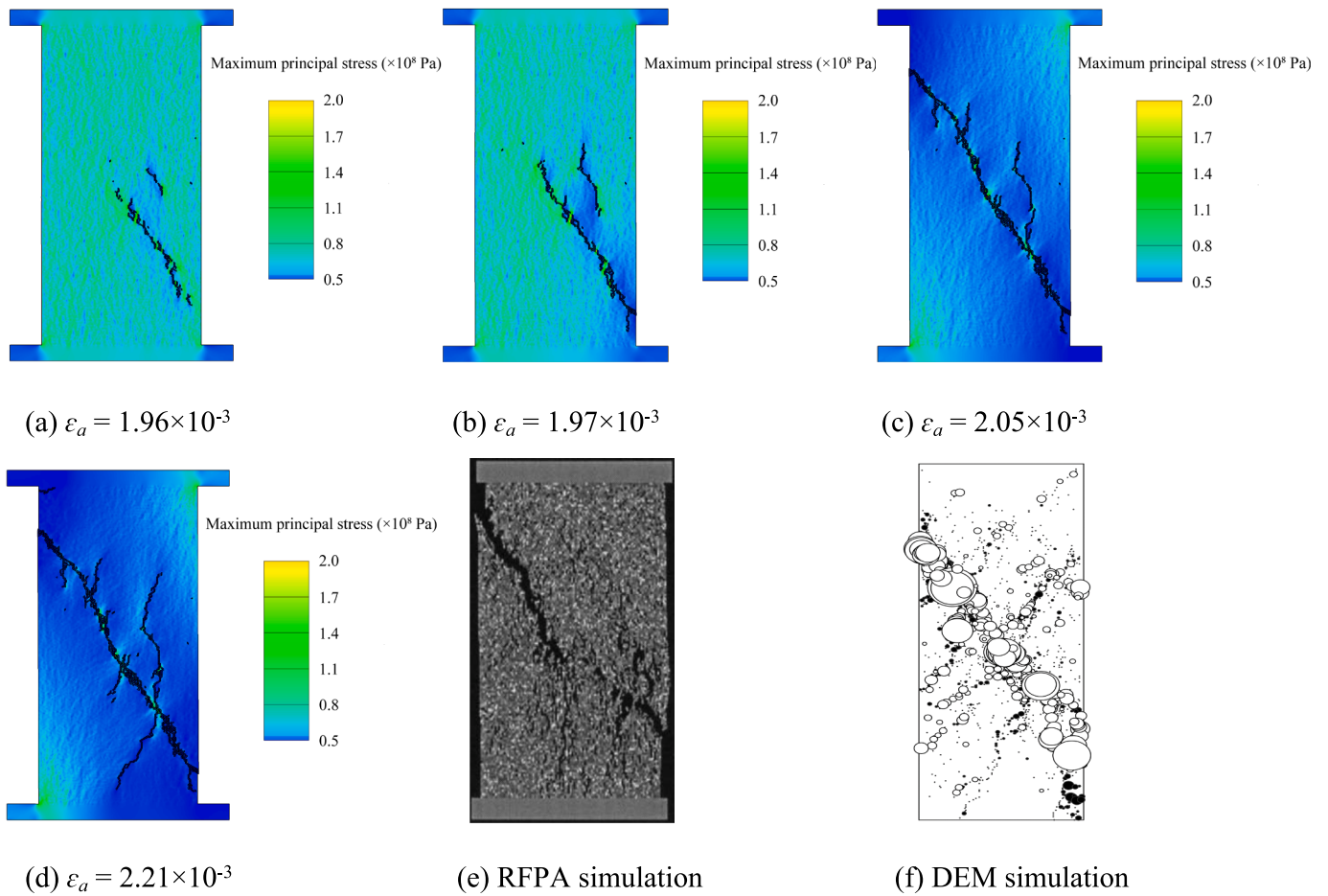


Fig. 12. Rock fracturing under uniaxial compression: (a)–(d) the crack initiation and propagation processes simulated by the proposed method; (e) the failure mode simulated by RFPA (Tang et al., 2000); (f) the failure mode simulated by DEM (Shimizu et al., 2010) (Note: ϵ_a represents the axial strain).

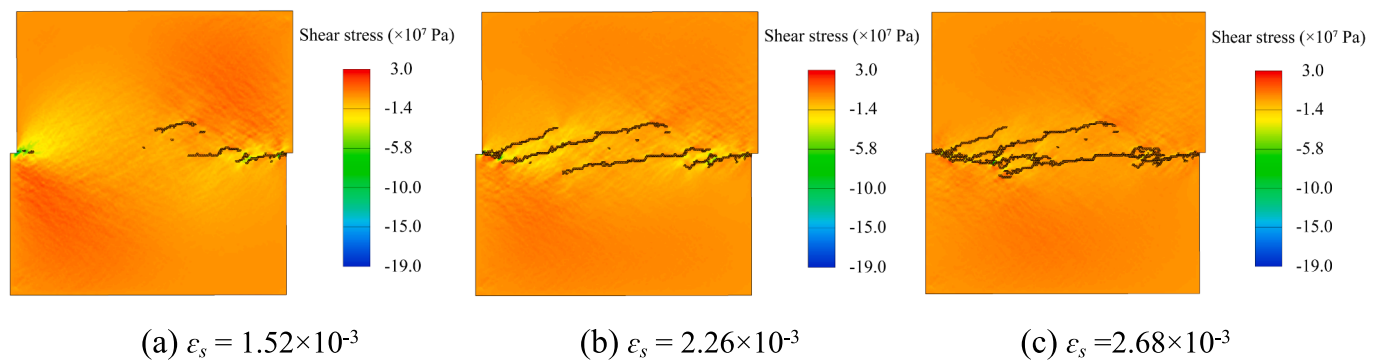


Fig. 13. Rock fracturing process under direct shear loading (Note: ϵ_s represents the shear strain).

Table 2

Physical-mechanical properties of the rock specimen for direct shear.

Parameter	Value
Elastic modulus E (GPa)	96.3
Poisson's ratio ν	0.3
Homogeneity coefficient m	5
Cohesion c (MPa)	53.7
Internal friction angle φ (°)	22.59°
Uniaxial tensile strength f_{t0} (MPa)	9.62

reached a certain level, the penetrating failure surface occurred. At this moment, the factor of safety (FoS) of the slope was determined as the ratio of the increased gravity to the original gravity. Subsequently, the gravity in the numerical model was kept constant during slope sliding.

Fig. 16 illustrates the progressive failure and mass spreading process of the slope. In Fig. 16 (a), it can be observed that as gravity increased, a set of micro-cracks was initiated at the slope toe region due to stress concentration. The shear zone gradually increased in size as the cracks propagated and nucleated towards the slope crest. Meanwhile, several tension cracks can be observed near the slope crest and inclined surface in Fig. 16 (b) due to tensile failure of mesh elements, which is the main feature of deep-seated slope failure. Fig. 16 (c) shows that an obvious

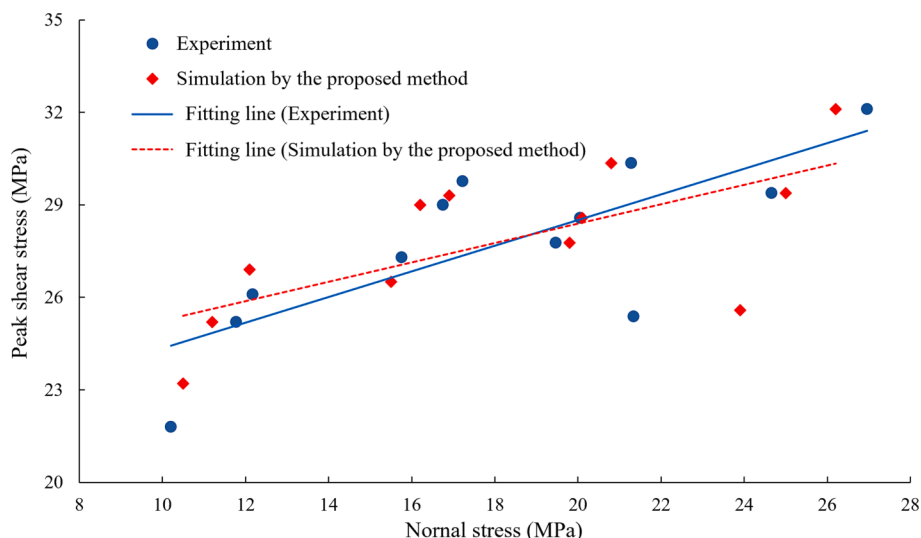


Fig. 14. Shear strength comparison between simulation and experiment.

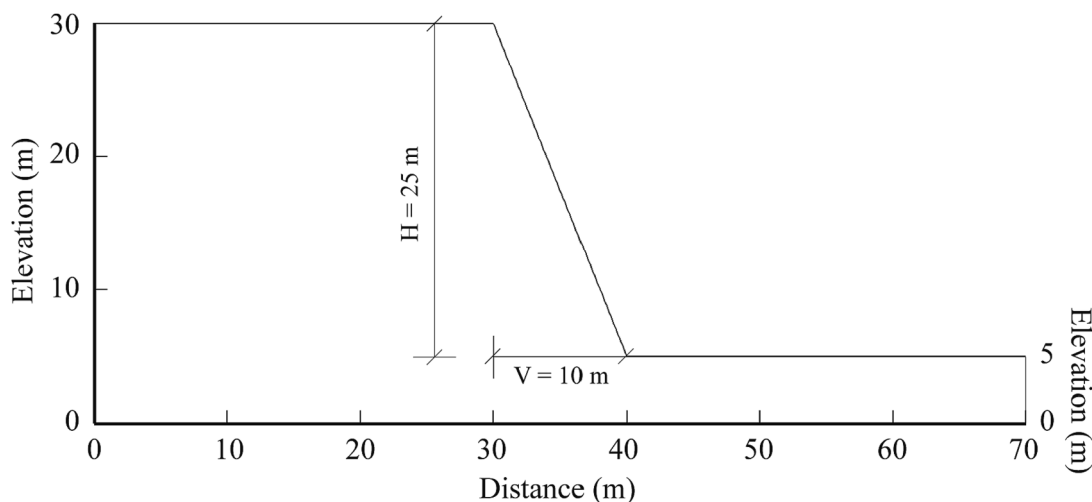


Fig. 15. Numerical model configuration of slope failure modelling.

Table 3
Physical-mechanical properties of the slope media.

Parameter	Value
Density ρ (kg/m ³)	2700
Elastic modulus E (GPa)	10
Poisson's ratio ν	0.25
Homogeneity coefficient m	5
Cohesion c (MPa)	1.1
Internal friction angle φ (°)	25°
Uniaxial tensile strength f_{t0} (MPa)	0.8

arc-shaped failure surface was finally formed as the major inner crack nucleated with the upper tension cracks, resulting in the formation of a large landslide body. Simultaneously, multiple major tension cracks within the sliding body split the rock mass into several large blocks.

In Fig. 16 (d) and (e), the mass spreading along the failure surface caused the blocks at the lower part of the sliding body to gradually separate from the main body due to rigid block displacement. Subsequently, in Fig. 16 (f), the large blocks at the lower part of the sliding body are further broken into smaller blocks due to strong squeezing and collision. However, the blocks at the upper part of the sliding body could still remain relatively intact, indicating that the sliding body is broken

into numerous small fragments, with some large rocks surviving until the late stage of sliding. These observed features are consistent with field observations of landslides (Yu et al., 2021).

To quantify the slope damage during the initial fracturing process (*i. e.*, before sliding), the cumulative number of damaged elements within the slope model is shown in Fig. 17. The slope damage started to occur at the load time of 0.6250 s. Then, the number of failed elements remained relatively small until the load time reached 0.6542 s. After that, the damaged elements increased rapidly within a short time from 0.6542 s to 0.6953 s until the interconnected failure plane was formed. It remained unchanged during the initial stage of sliding, and as expected, more damage would occur during the subsequent land sliding and collision, as shown in Fig. 16 (e) and (f).

To understand the influence of material heterogeneity on the formation of failure surface, the same model configuration and loading history were applied to models with homogeneity coefficients set to 5, 8, and 11, respectively. These values represent slopes with increasing homogeneous material properties. The simulation was repeated 20 times to account for possible variations in slope responses for each input homogeneity coefficient. The results are shown in Fig. 18.

From Fig. 18, it is evident that a wide spread distribution of failure surfaces existed, indicating the variability and uncertainty of natural

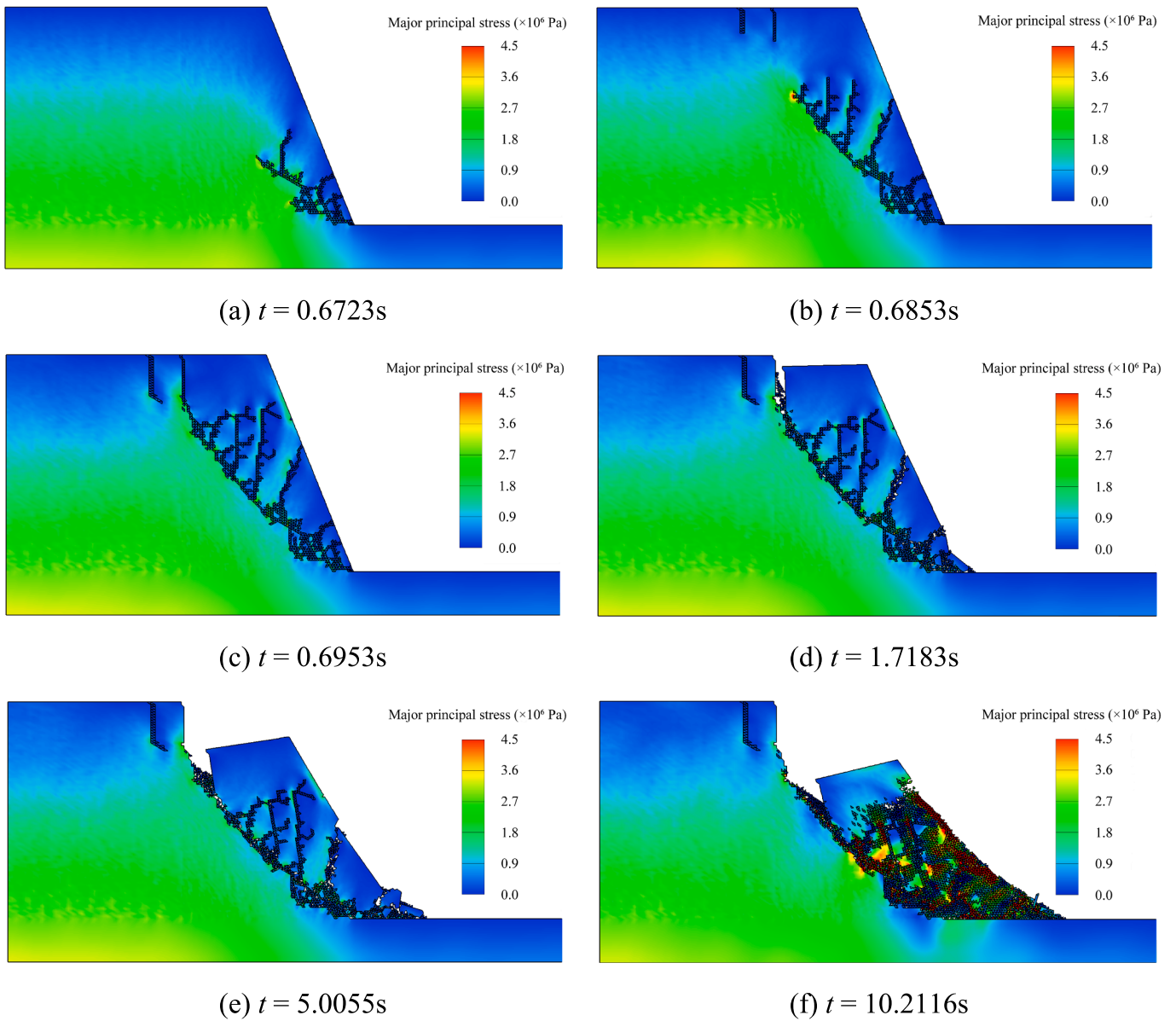


Fig. 16. Snapshots of progressive slope failure and evolution mass spreading.

slope failure. Near the slope toe region, material heterogeneity had little influence on the failure pattern, and these curves were closely distributed. However, near the slope crest zone, the locations of tension cracks showed great scattering, and the failed zone became increasingly wider as the homogeneity coefficient increased. This phenomenon was because slopes with relatively homogeneous material properties had more integrated structures that could better resist shallow slope failures. The final failure mode at higher gravity loading tended to be deep-seated large-scale landslides. For tests with low homogeneity coefficients, many weak elements existed in the model, resulting in easy failure under gravity loading and shallow slope surface failures.

Fig. 18 (b) summarized the mean FoS for all tests using different homogeneity coefficients (m). It could be observed that the value of FoS increased quickly during the initial growth stage of homogeneity coefficient, but it remained stable for relatively uniform slopes when m exceeded 8. The overall trend could be best fitted with a logarithmic function for heterogeneous slopes, *i.e.*, $\text{FoS} = 1.0935\ln(m) + 2.3764$ ($m < 8$), followed by a linear function for relatively homogeneous slopes, *i.e.*, $\text{FoS} = 0.0167 \times m + 4.8346$ ($m \geq 8$).

Furthermore, to investigate the influence of slope height on the slope

failure mode, a series of simulations were conducted using the numerical model with the same slope inclination but different heights. The homogeneity coefficient was kept constant at 5, and the slope heights were set to 10.0 m, 17.5 m, and 25.0 m, respectively. For each slope height, 20 simulations were run. Fig. 19 (a) shows the comparison of the obtained failure surface distribution as affected by different slope heights. It can be observed that the location of tension cracks at the slope crest gradually moved leftwards with increasing slope height. This phenomenon was due to the fact that the upper part of a sliding surface is generally caused by tensile failure, while the middle and lower parts are induced by compression-shear failure. The length of the shear-resistant surface increased with the rising slope height, leading to the backward movement of tensile failure areas. Meanwhile, when the slope height was small, the upper part of the failure band was relatively narrow, while it became wider as the slope height increased. This phenomenon was attributed to the high tensile stress concentrations being limited to a small area at the back of the slope with decreasing slope height, resulting in narrower potential failure paths. Fig. 19 (b) shows that the factor of slope safety decreased with the increase of the ratio of the slope height (h) to the width (w) of the crest surface, following a power law function

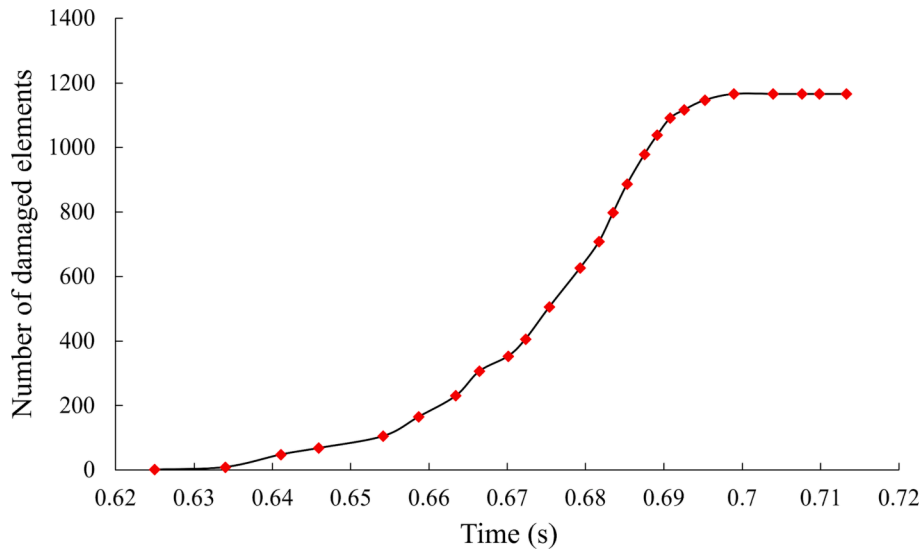


Fig. 17. Number of damaged elements during the formation of slope failure surface.

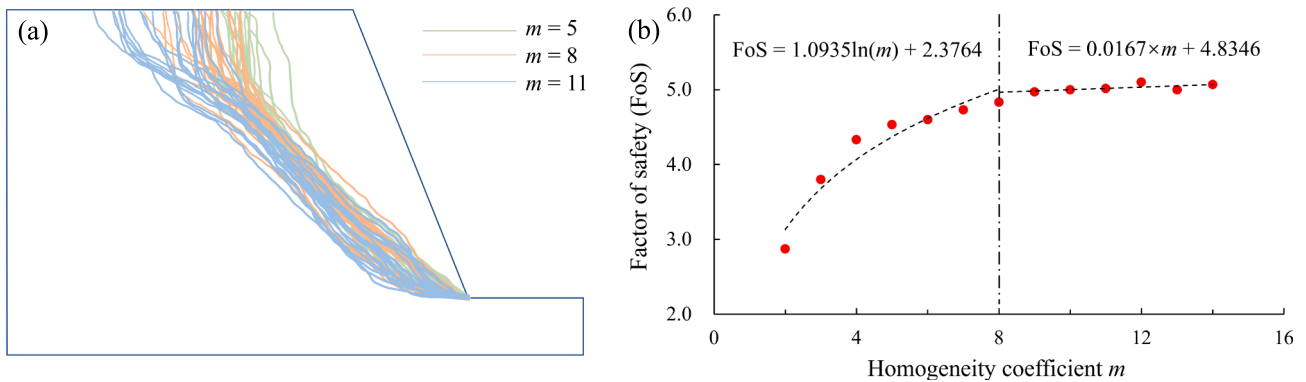


Fig. 18. Influence of the material heterogeneity on (a) the location of failure surface and (b) the factor of safety.

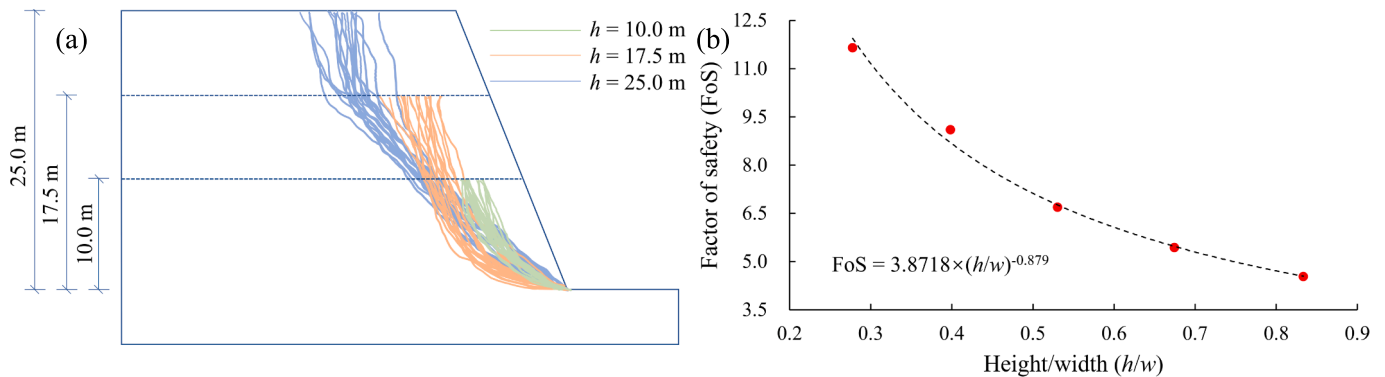


Fig. 19. Influence of the slope height on (a) the failure surface and (b) the factor of safety.

as $FoS = 3.8718 \times (h/w)^{-0.879}$.

5. Conclusions

In this study, a novel implicit continuous to discontinuous method was proposed based on the rock mechanics, computational mechanics, and contact mechanics. This newly developed method was then used to investigate the cross-scale failure process of discontinuous rock mass, involving fine fracture creation, propagation, and penetration. The

major conclusions of this study can be summarized as follows:

- (1) The potential energy equations associated with all forces or stresses, including strain, initial stress, point load, volume load, inertia force, contact spring strain, and friction, were deduced. The partial derivative equations of each potential energy component along the x-axis and y-axis were calculated. Specifically, submatrices induced by normal spring, tangential spring, and friction were derived to capture the mechanical contact

between adjacent blocks. Subsequently, the manner in which these obtained submatrices can be incorporated into the corresponding positions of the global equilibrium equation was determined. In the developed method, the change of each potential energy component at each time step can be updated, and the system can automatically reach equilibrium by solving the global equilibrium equation.

- (2) In the proposed program, an intact rock is endowed with the ability to split and crush. Initially, the rock can deform in various forms under applied loads. As the load increases, and the strength criterion is satisfied, new crack initiation or crack propagation can occur within the rock. With further increase in load, the rock can be fragmented into smaller pieces due to the coalescence of new cracks. The boundaries of these small rocks are contactable, allowing for opening, sliding, and locking to occur. Especially, when a grid line becomes a joint, its adjacent elements on both sides are separated, and the contact boundaries in the new mesh are updated by the developed searching algorithm.
- (3) The proposed method has proven to be effective in modeling the progressive failure process of slopes. It is observed that high concentrated stresses can trigger crack initiation, and the continuous process of crack propagation and nucleation ultimately leads to slope failure. The number of failure elements within the slope increased rapidly during the primary fracture stage. The lower part of the sliding body is susceptible to fragmentation into smaller blocks due to strong squeezing and collision, while some larger and harder rocks may remain intact until the later stages of sliding.
- (4) The failed zone widened and the factor of safety (FoS) increased as the homogeneity coefficient increased. FoS remained an almost constant value when m exceeded 8, indicating a relatively uniform material behavior. Notably, in slopes with varying elevation heights, the FoS decreased in a power function form with an increasing ratio of slope height to the width of the slope crest surface. Besides, because of the solving overhead at each time step, the proposed method can be computationally expensive for highly non-linear questions. Simultaneously, the computational efficiency depends on the total number and length of cracks existing inside a numerical model and is influenced by the cracking degree during calculation. Additionally, the proposed method has limitations in dealing with fine cracks considering that cracks are modelled at the element level. These questions need further investigation.

CRediT authorship contribution statement

Bin Gong: Formal analysis, Investigation, Methodology, Software, Validation, Writing – original draft, Writing – review & editing. **Tao Zhao:** Conceptualization, Funding acquisition, Project administration, Supervision, Writing – review & editing. **Indrasenan Thusyanthan:** Conceptualization, Supervision. **Chun'an Tang:** Conceptualization, Software.

Declaration of Competing Interest

The authors declare that they have no known competing financial interests or personal relationships that could have appeared to influence the work reported in this paper.

Data availability

The datasets generated and/or analyzed during the current study are available from the corresponding author upon reasonable request.

Acknowledgements

The authors would like to express their gratitude for the financial support provided by the UK Engineering and Physical Sciences Research Council (EPSRC) New Investigator Award (Grant No. EP/V028723/1).

References

- Basu, B., Tiwari, D., Kundu, D., Prasad, R., 2009. Is Weibull distribution the most appropriate statistical strength distribution for brittle materials? *Ceram. Int.* 35 (1), 237–246.
- Belytschko, T., Organ, D., Gerlach, C., 2000. Element-free galerkin methods for dynamic fracture in concrete. *Comput. Methods Appl. Mech. Eng.* 187 (3), 385–399.
- Bishop, A.W., 1955. The use of the slip circle in stability analysis of slope. *Geotechnique* 5 (1), 7–17.
- Brady, B.H.G., Bray, J.W., 1978. Boundary element method for determining stresses and displacements around long openings in a triaxial stress-field. *Int. J. Rock Mech. Min. Sci.* 15 (1), 21–28.
- Chen, B., Barron, A.R., Owen, D.R.J., Li, C.F., 2018a. Propagation of a plane strain hydraulic fracture with a fluid lag in permeable rock. *J. Appl. Mech.* 85 (9), 091003.
- Chen, B., Cen, S., Barron, A.R., Owen, D.R.J., Li, C.F., 2018b. Numerical investigation of the fluid lag during hydraulic fracturing. *Eng. Comput.* 35 (5), 2050–2077.
- Chen, B., Xiang, J.S., Latham, J.P., Bakker, R.R., 2020. Grain-scale failure mechanism of porous sandstone: an experimental and numerical FDEM study of the Brazilian Tensile Strength test using CT-Scan microstructure. *Int. J. Rock Mech. Min. Sci.* 132, 104348.
- Chen, B., Barboza, B.R., Sun, Y.N., Bai, J., Thomas, H.R., Dutko, M., Cottrell, M., Li, C.F., 2022a. A review of hydraulic fracturing simulation. *Arch. Comput. Meth. Eng.* 29, 1–58.
- Chen, T.T., Foulger, G.R., Tang, C.A., Mathias, S.A., Gong, B., 2022b. Numerical investigation on origin and evolution of polygonal cracks on rock surfaces. *Eng. Geol.* 311, 106913.
- Cheng, Y.M., 1998. Advancements and improvement in discontinuous deformation analysis. *Comput. Geotech.* 22 (2), 153–163.
- Cundall, P.A., 1971. A computer model for simulating progressive large scale movements in blocky rock systems. In: *Proceedings of the symposium of the International Society for Rock Mechanics (ISRM)*, Nancy, France.
- Deb, D., Pramanik, R., Das, K.C., 2015. A generalized XFEM procedure for analyzing intersecting joints in rock masses with excavation. *Eng. Comput.* 32 (3), 806–833.
- Deng, L., Li, X., Wu, Y., Li, F., Huang, Z., Ji, Y., Zou, C., Liu, Z., 2022. Influence of cooling speed on the physical and mechanical properties of granite in geothermal-related engineering. *Deep Undergr. Sci. Eng.* 1 (1), 40–57.
- Doolin, D.M., Sitar, N., 2002. Displacement accuracy of discontinuous deformation analysis method applied to sliding block. *J. Eng. Mech.* 128 (11), 1158–1168.
- Fallah, N.A., Bailey, C., Cross, M., Taylor, G.A., 2000. Comparison of finite element and finite volume methods application in geometrically nonlinear stress analysis. *App. Math. Model.* 24 (7), 439–455.
- Fellenius, W., 1936. Calculation of the stability of earth dams. In: *Proceedings of the Second Congress on Large Dams, International Commission on Large Dams of the Word Power Conference, Washington D.C., US*.
- Feng, X.H., Gong, B., Cheng, X.F., Zhang, H.H., Tang, C.A., 2022. Anisotropy and microcrack-induced failure precursor of shales under dynamic splitting. *Geomat. Nat. Haz. Risk* 13 (1), 2864–2889.
- Fries, T.P., Belytschko, T., 2010. The extended/generalized finite element method: an overview of the method and its applications. *Int. J. Numer. Meth. Eng.* 84 (3), 253–304.
- Fu, J.W., Zhang, X.Z., Zhu, W.S., Chen, K., Guan, J.F., 2017. Simulating progressive failure in brittle jointed rock masses using a modified elastic-brittle model and the application. *Eng. Fract. Mech.* 178, 212–230.
- Ghaboussi, J., Wilson, E.L., Isenberg, J., 1973. Finite element for rock joints and interfaces. *J. Soil Mech. Found. Div.* 99 (SM10), 833–848.
- Gong, B., Liang, Z.Z., Liu, X.X., 2022. Nonlinear deformation and failure characteristics of horseshoe-shaped tunnel under varying principal stress direction. *Arab. J. Geosci.* 15, 475.
- Gong, B., Tang, C.A., 2016. Slope-slide simulation with discontinuous deformation and displacement analysis. *Int. J. Geomech.* 17 (5), E4016017.
- Gong, B., Wang, S.Y., Sloan, S.W., Sheng, D.C., Tang, C.A., 2018. Modelling coastal cliff recession based on the GIM-DDD method. *Rock Mech. Rock Eng.* 51 (4), 1077–1095.
- Gong, B., Tang, C.A., Wang, S.Y., Bai, H.M., Li, Y.C., 2019. Simulation of the nonlinear mechanical behaviors of jointed rock masses based on the improved discontinuous deformation and displacement method. *Int. J. Rock Mech. Min. Sci.* 122, 104076.
- Goodman, R.E., 1976. *Methods of Geological Engineering in Discontinuous Rocks*. West Publishing Company, San Francisco.
- Goodman, R.E., Taylor, R.L., Brekke, T.L., 1968. A model for the mechanics of jointed rock. *J. Soil Mech. Found. Div.* 94, 637–659.
- Guo, L., Latham, J.P., Xiang, J., 2017. A numerical study of fracture spacing and through-going fracture formation in layered rocks. *Int. J. Solids Struct.* 110–111, 44–57.
- Guo, L., Xiang, J., Latham, J.P., Izzuddin, B., 2020. A generic computational model for three-dimensional fracture and fragmentation problems of quasi-brittle materials. *Eur. J. Mech.-A/Solids* 84, 104069.
- Guo, H., Zheng, H., Zhuang, X., 2019. Numerical manifold method for vibration analysis of Kirchhoff's plates of arbitrary geometry. *App. Math. Model.* 66, 695–727.
- Ha, Y.D., Lee, J., Hong, J.W., 2015. Fracturing patterns of rock-like materials in compression captured with peridynamics. *Eng. Fract. Mech.* 144, 176–193.

- Harrison, J.P., Hudson, J.A., 1997. *Engineering Rock Mechanics Part I: An Introduction to the Principles*. Pergamon, Oxford.
- Hoxha, D., Homand, F., 2000. Microstructural approach in damage modeling. *Mech. Mater.* 32 (6), 377–387.
- Janbu, N., 1973. *Slope stability computations*. In: Hirschfield, R.C., Poulos, S.J. (Eds.). John Wiley and Sons Inc., NY, pp. 47–86.
- Kachanov, L.M., 1999. Rupture time under creep conditions. *Int. J. Fract.* 97 (1), 11–18.
- Li, S., Qian, D., Liu, W.K., Belytschko, T., 2001. A meshfree contact-detection algorithm. *Comput. Methods Appl. Mech. Eng.* 190, 3271–3292.
- Li, G., Wang, K., Gong, B., Tao, Z.G., Du, K., 2021. A multi-temporal series high-accuracy numerical manifold method for transient thermoelastic fracture problems. *Int. J. Solids Struct.* 230–231, 111151.
- Li, H., Wong, L.N.Y., 2012. Influence of flaw inclination angle and loading condition on crack initiation and propagation. *Int. J. Solids Struct.* 49 (18), 2482–2499.
- Liang, Z.Z., 2005. *Three-dimensional Failure Process Analysis of Rock and Associated Numerical Tests*. Northeastern University, Shenyang, China. Ph.D.
- Liang, Z.Z., Gong, B., Tang, C.A., Zhang, Y.B., Ma, T.H., 2014. Displacement back analysis for a high slope of the Dagangshan Hydroelectric Power Station based on BP neural network and particle swarm optimization. *Sci. World J.* 2014, 741323.
- Long, J.C.S., Remer, J.S., Wilson, C.R., Witherspoon, P.A., 1982. Porous media equivalent for networks of discontinuous fractures. *Water Resour. Res.* 18, 645–658.
- Long, J.C.S., Gilmour, P., Witherspoon, P.A., 1985. A model for steady fluid flow in random three-dimensional networks of disc-shaped fractures. *Water Resour. Res.* 21 (8), 1105–1115.
- Luo, S., Gong, F., 2022. Evaluation of rockburst proneness considering specimen shape by storable elastic strain energy. *Deep Undergr. Sci. Eng.* 1 (2), 116–130.
- Ma, Z., Zheng, Y., He, L., Li, J., 2022. Effect of joints on microwave fracturing of the Bukit Timah granite using an open-ended antenna. *Deep Undergr. Sci. Eng.* 1 (2), 138–147.
- Manthei, G., 2005. Characterization of acoustic emission sources in a rock salt specimen under triaxial compression. *Bull. Seismol. Soc. Am.* 95 (5), 1674–1700.
- Meglis, I.L., Chows, T.M., Young, R.P., 1995. Progressive microcrack development in tests in Lac du Bonnet granite-I. Acoustic emission source location and velocity measurements. *Int. J. Rock Mech. Min. Sci. Geomech. Abstr.* 32, 741–750.
- Morgenstern, N.R., Price, V.E., 1965. The analysis of the stability of general slip surface. *Geotechnique* 15, 70–93.
- Nassar, M., Afify, A.Z., Dey, S., Kumar, D., 2018. A new extension of Weibull distribution: properties and different methods of estimation. *J. Comput. Appl. Math.* 336, 439–457.
- Rice, J., 1968. A path independent integral and the approximate analysis of strain concentration by notched and cracks. *J. Appl. Mech.* 35, 379–386.
- Robinson, P.C., 1984. *Connectivity, Flow and Transport in Network Models of Fractured Media*. University of Oxford, Oxford, UK. Ph.D.
- Rodrigo, C., Gaspar, F.J., Hu, X., Zikatanov, L., 2015. A finite element framework for some mimetic finite difference discretizations. *Comput. Math. Appl.* 70 (11), 2661–2673.
- Rutqvist, J., Borgesson, L., Chijimatsu, M., Kobayashi, A., Jing, L., Nguyen, T.S., Noorishad, J., Tsang, C.F., 2001. Thermohydromechanics of partially saturated geological media: governing equations and formulation of four finite element models. *Int. J. Rock Mech. Min. Sci.* 38 (1), 105–127.
- Rybicki, E.F., Kanninen, M.F., 1977. A finite element calculation of stress intensity factors by a modified crack closure integral. *Eng. Fract. Mech.* 9 (4), 931–938.
- Sanchidrian, J.A., Ouchterlony, F., Segarra, P., Moser, P., 2014. Size distribution functions for rock fragments. *Int. J. Rock Mech. Min. Sci.* 71, 381–394.
- Shi, G.H., 1988. *Discontinuous Deformation Analysis: A New Numerical Model for the Statics and Dynamics of Block Systems*. University of California, Berkeley, US. Ph.D.
- Shi, G.H., 2015. Contact theory. *Sci. China Technol. Sci.* 58 (9), 1450–1496.
- Shimizu, H., Koyama, T., Ishida, T., Chijimatsu, M., Fujita, T., Nakama, S., 2010. Distinct element analysis for Class II behavior of rocks under uniaxial compression. *Int. J. Rock Mech. Min. Sci.* 47 (2), 323–333.
- Spencer, E., 1967. A method of analysis of the stability of embankments assuming parallel inter-slice forces. *Geotechnique* 17, 11–26.
- Strouboulis, T., Babuška, I., Copps, K., 2000. The design and analysis of the generalized finite element method. *Comput. Methods Appl. Mech. Eng.* 181 (1), 43–69.
- Strouboulis, T., Copps, K., Babuška, I., 2001. The generalized finite element method. *Comput. Methods Appl. Mech. Eng.* 190 (32), 4081–4193.
- Tang, C.A., 1997. Numerical simulation of progressive rock failure and associated seismicity. *Int. J. Rock Mech. Min. Sci.* 34 (2), 249–261.
- Tang, C.A., Liu, H., Lee, P.K.K., Tsui, Y., Tham, L.G., 2000. Numerical studies of the influence of microstructure on rock failure in uniaxial compression-Part I: effect of heterogeneity. *Int. J. Rock Mech. Min. Sci.* 37 (4), 555–569.
- Tang, C.A., Tham, L.G., Lee, P.K.K., Yang, T.H., Li, L.C., 2002. Coupled analysis of flow, stress and damage (FSD) in rock failure. *Int. J. Rock Mech. Min. Sci.* 39 (4), 477–489.
- Tang, C.A., Tang, S.B., Gong, B., Bai, H.M., 2015. Discontinuous deformation and displacement analysis: from continuous to discontinuous. *Sci. China Technol. Sci.* 58 (9), 1567–1574.
- Wang, Y., Gong, B., Zhang, Y., Yang, X., Tang, C., 2022a. Progressive fracture behavior and acoustic emission release of CJBs affected by joint distance ratio. *Mathematics* 10, 4149.
- Wang, Y., Gong, B., Tang, C.A., 2022b. Numerical investigation on anisotropy and shape effect of mechanical properties of columnar jointed basalts containing transverse joints. *Rock Mech. Rock Eng.* 55, 7191–7222.
- Weibull, W., 1951. Wide applicability. *J. Appl. Mech.* 103 (730), 293–297.
- Wheel, A.M., 1996. A geometrically versatile finite volume formulation for plane elastostatic stress analysis. *J. Strain Anal. Eng. Des.* 31, 111–116.
- Xiang, J.S., Chen, B., Latham, J.P., Pain, C., 2022. Numerical simulation of rock erosion performance of a high-speed water jet using an immersed body method. *Int. J. Rock Mech. Min. Sci.* 158, 105179.
- Yang, Y., Tang, X., Zheng, H., Liu, Q., Liu, Z., 2018. Hydraulic fracturing modeling using the enriched numerical manifold method. *App. Math. Model.* 53, 462–486.
- Yu, X., Gong, B., Tang, C.A., 2021. Study of the slope deformation characteristics and landslide mechanisms under alternating excavation and rainfall disturbance. *Bull. Eng. Geol. Environ.* 80 (9), 7171–7191.
- Yu, C.Y., Gong, B., Wu, N., Xu, P.L., Bao, X.K., 2022. Simulation of the fracturing process of inclusions embedded in rock matrix under compression. *Appl. Sci.* 12 (16), 8041.
- Zhang, F., Cui, L., An, M., Elsworth, D., He, C., 2022. Frictional stability of Longmaxi shale gouges and its implication for deep seismic potential in the southeastern Sichuan Basin. *Deep Undergr. Sci. Eng.* 1 (1), 3–14.
- Zhang, X., Lu, M., L. Wegner J., 2000. A 2-D meshless model for jointed rock structures. *Int. J. Numer. Meth. Eng.* 47, 1649–1661.
- Zhang, G., Yang, Y., Zheng, H., 2018. A mass lumping scheme for the second-order numerical manifold method. *Comput. Struct.* 213, 23–29.